



AIAA 2002-1717

Flutter Suppression for High Aspect Ratio
Flexible Wings Using Microflaps

Hak-Tae Lee, Ilan M. Kroo, and Stefan Bieniawski
Stanford University
Stanford, CA 94305

Structural Dynamics, and Material Conference
22–25 April 2002
Denver, Colorado

Flutter Suppression for High Aspect Ratio Flexible Wings Using Microflaps

Hak-Tae Lee, * Ilan M. Kroo †
 Stefan Bieniawski ‡
Stanford University, Stanford, CA 94305

Abstract

Miniature trailing edge effectors (MiTEs) are small flaps (typically 1% to 5% chord) actuated with deflection angles up to 90 degrees. Because of their small size, these devices provide the opportunity for high bandwidth control. The present study considers the use of many such control surfaces to increase the flutter speed of a high aspect ratio flexible wing. A finite element plate model is used to model the structural dynamics and an unsteady panel method provides the aerodynamic loads. Experimental flutter testing shows good agreement with the numerical stability analysis. The MiTE is modelled by a single panel element at the trailing edge with varying boundary conditions at its collocation point. In spite of the complex viscous aerodynamics of the MiTEs, the panel model proved to be adequate in simulating the steady and unsteady behavior. The use of these effectors for control is complicated by their nonlinear characteristics. Since the actuator is only effective at high deflection angles, it is only deflected in one of three positions: up, down, and neutral. The design of a nonlinear feedback controller has been performed using numerical optimization.

Introduction

The Gurney flap is a small (typically 1% ~ 5% chord) flap used to increase the maximum lift of an airfoil section. It was developed and applied to racing cars by Robert Liebeck and Dan Gurney in 1960's, although similar devices were employed in World War II aircraft such as the P-38

and F8-F. Numerous wind-tunnel tests and numerical computations have been conducted on both single element and multi-element airfoils with Gurney flaps.¹⁻⁶ These studies confirm that despite their small size, Gurney flaps with deflections near 90 degrees can increase maximum lift and the lift produced at a given angle of attack. Liebeck¹ explained this effect, produced by a short region of separated flow directly upstream of the flap, with two counter-rotating vortices downstream that effectively modify the trailing edge Kutta condition. This was verified to be correct for time averaged flow by flow visualizations^{5,6} and CFD² simulations.

In the present work, we consider the use of devices similar to Gurney flaps, not to increase maximum lift, but to provide high bandwidth, robust control. Miniature Trailing edge Effectors (MiTEs) are small movable control surfaces at or near the trailing edge, deflected to large angles to produce control forces and moments that may be used for flight control or structural mode control. The current study, begun in 1998,⁷ deals with the use of such actuators for aeroelastic control.

MiTEs have distinct advantages over conventional control surfaces: High bandwidth actuation can be achieved due to their small size and inertia, enabling their use for flight control or for higher frequency structural mode control with significantly reduced power requirements. Spanwise variation and interdigitated deflections can produce rolling, pitching, and yawing moments, as well as the control of specific structural modes. Because the surfaces are deflected in a discrete manner (up, down, or neutral), no active servo-feedback is required, eliminating the expense of accurate, high-rate servo actuators and enabling a large number of these effectors to be fabricated at a low cost. The use of a large number of small, simple effectors also makes the system fault-tolerant.

The application of MiTEs for aeroelastic control is demonstrated here by designing an active control system that can suppress the flutter of a flexible wing. High aspect ratio flexible wings are of interest

*Doctoral Candidate, Department of Aeronautics and Astronautics, AIAA Student Member

†Professor, Department of Aeronautics and Astronautics, AIAA Fellow

‡Doctoral Candidate, Department of Aeronautics and Astronautics, AIAA Member

Copyright ©2002 by authors. Published by the American Institute of Aeronautics and Astronautics, Inc., with permission.

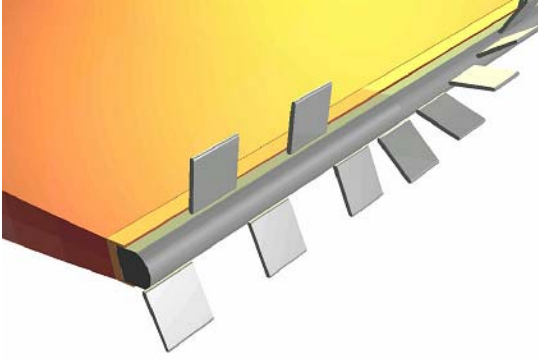


Figure 1: Array of MiTEs

in many applications including unmanned aerial vehicles for which aeroelastic stability is an important consideration.

A model that combines a finite element method for structural dynamics and an unsteady vortex panel method for aerodynamics was developed to study the use of MiTEs for aeroelastic control. This model was used to analyze a thin composite wing designed to meet flutter speed and frequency constraints imposed by the wind tunnel and actuator characteristics. The wing was fabricated and a wind tunnel experiment was conducted to verify the computed flutter and divergence speeds for the model. Results agreed well with the numerical stability analysis.

In the current work each actuator is deflected in one of two states, either neutral-up or neutral-down, and a set of 26 devices are attached along the entire trailing edge. With the combined aero/structural model several control schemes were investigated to increase the flutter speed of the wing. With a localized control law that feeds back the local deflection and rate of twist to the local flap, gains were determined using nonlinear optimization. With this controller, flutter speed could be increased by up to 22%, a 49% increase in the dynamic pressure.

Structural Model

As part of an on-going effort to experimentally demonstrate flutter suppression using MiTEs, a wind tunnel model was fabricated and preliminary tests have been completed. Although the experimental effort is not the focus of this paper, the results of the preliminary tests will be used to validate the analysis model presented in this paper. In addition, the choice of modelling approaches, in particular for the structure, was dictated by the experimental model.

E_1	7.4250×10^9 Pa
E_2	7.4250×10^9 Pa
ν_{12}	0.17
ρ	1217 Kg/m ³
t_{ply}	1.7426×10^{-4} m
Stacking sequence	$[0_6/\pm 45]_s$

Table 1: Material and laminate properties for experimental model

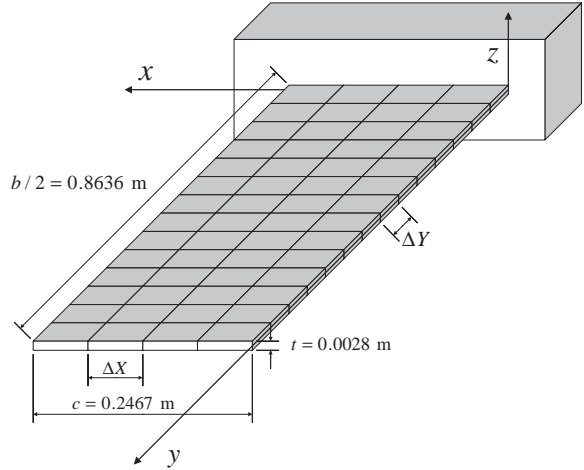


Figure 2: Perspective view of wing with FEM grid

The experimental model consists of a rectangular laminated fiberglass flat plate. The model measures 0.8636 m by 0.2467 m by 0.0028 m and consists of 16 plies of wet layup fiberglass fabric. The model is cantilevered at the base and can be set at varying angles of sweep. For the current study, no sweep was considered. The stacking sequence for the laminate was determined to ensure aeroelastic behavior consistent with the capabilities of the MiTE actuators (e.g. flutter frequency) and of the Stanford Flow Control Wind Tunnel (e.g. flutter speed). Table 1 details the material properties and lamination sequence. The material properties shown in Table 1 represent values updated following initial vibration tests. The experimentally determined natural frequencies of the first three modes are shown in Table 2. The experimental model exhibited flutter at 14 m/s with a flutter frequency of 5 Hz.

A four node twelve degree of freedom rectangular bending element is used in finite element formulation. Figure 2 shows the perspective view of the wing with all elements and dimensions. Using four chordwise elements and fourteen spanwise elements was sufficient to obtain good results.

The detailed finite element formulation can be

found in Prezmieniecki¹¹ including the vector of shape functions, $\mathbf{a}(x, y)$, for the selected element.

$$u_z(x, y) = \mathbf{a}(x, y)^T \mathbf{u}_{node} \quad (1)$$

Using the expressions for the strains, the nodal degrees of freedom are related to the strains in the plate element through:

$$\epsilon_{xx} = -z \frac{\partial^2 u_z}{\partial x^2}, \epsilon_{yy} = -z \frac{\partial^2 u_z}{\partial y^2}, \epsilon_{xy} = -2z \frac{\partial^2 u_z}{\partial x \partial y} \quad (2)$$

$$\epsilon(x, y, z) = \mathbf{b}(x, y, z) \mathbf{u}_{node} \quad (3)$$

$$= z \hat{\mathbf{b}}(x, y) \mathbf{u}_{node} \quad (4)$$

From the strain distribution $\hat{\mathbf{b}}$ and the out of plane composite plate stiffness \mathbf{D} , the stiffness matrix becomes

$$\mathbf{K}_e = \int_x \int_y \hat{\mathbf{b}}^T \mathbf{D} \hat{\mathbf{b}} dy dx \quad (5)$$

where

$$\mathbf{D} = \frac{1}{3} \sum_{k=1}^n Q_{ij}^k (h_k^3 - h_{k-1}^3) \quad (6)$$

Similarly, the element mass matrix is determined using the shape functions.

$$\mathbf{M}_e = \int_{V_e} \rho \mathbf{a} \mathbf{a}^T dV \quad (7)$$

The nodal forces are obtained from the aerodynamic load calculation. The pressure differences at the panels is translated to nodal forces using the equivalent work load method. The nodal forces exerting the same amount of work on each element as the distributed pressures are found by incorporating the shape functions.

$$\mathbf{F}_{N_e} = \iint_{element} \Delta P(x, y) \mathbf{a}^T(x, y) dx dy \quad (8)$$

After assembling all the element mass and stiffness matrices and applying the boundary condition, the continuous time equation of the motion becomes,

$$\mathbf{M}_g \ddot{\mathbf{x}} + \mathbf{C}_g \dot{\mathbf{x}} + \mathbf{K}_g \mathbf{x} = \mathbf{F}_{N_g} \quad (9)$$

Where \mathbf{C}_g is the modal damping matrix. The damping is added to suppress the high frequency

Mode	Frequency (FEM)	Frequency (Experiment)	Type
1st	1.49 Hz	1.49 Hz	1st Bending
2nd	7.71 Hz	8.24 Hz	1st Torsion
3rd	9.37 Hz	9.32 Hz	2nd Bending
4th	24.65 Hz		2nd Torsion
5th	26.29 Hz	30.22 Hz	3rd Bending

Table 2: Natural frequencies and modes of the composite wing

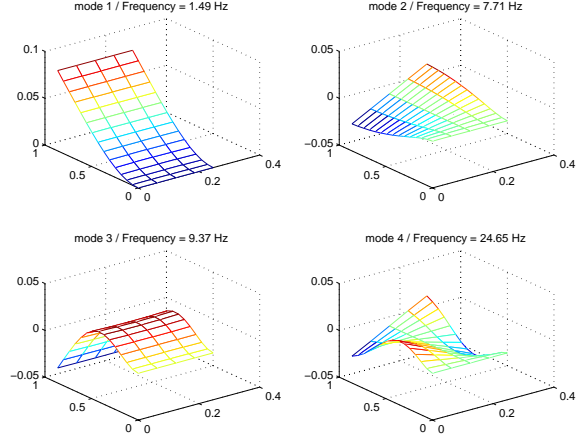


Figure 3: Mode shapes at natural vibration

modes which may become unstable because of numerical truncation errors. To accomplish this proportional damping was used, where the damping ratio of each mode is proportional to its modal frequency.

$$\zeta_i = \zeta_{max} \frac{\omega_{n_i}}{\omega_{n_{max}}} \quad (10)$$

A prescribed maximum damping ratio of 0.5 for the highest frequency mode was specified.

In order to combine this structural dynamic equation with the aerodynamic formulation which is in the discrete time domain, a central difference scheme is applied to the continuous time equations of motion, Equation 9.

$$\mathbf{q} = \begin{bmatrix} \dot{\mathbf{x}} \\ \mathbf{x} \end{bmatrix} \quad (11)$$

$$\mathbf{q} = \frac{\mathbf{q}^{n+1} + \mathbf{q}^n}{2}, \quad \dot{\mathbf{q}} = \frac{\mathbf{q}^{n+1} - \mathbf{q}^n}{\Delta t} \quad (12)$$

Starting with the state space form,

$$\begin{bmatrix} \mathbf{M}_g & \mathbf{C}_g \\ \mathbf{O} & \mathbf{M}_g \end{bmatrix} \begin{bmatrix} \ddot{\mathbf{x}} \\ \dot{\mathbf{x}} \end{bmatrix} + \begin{bmatrix} \mathbf{O} & \mathbf{K}_g \\ -\mathbf{M}_g & \mathbf{O} \end{bmatrix} \begin{bmatrix} \dot{\mathbf{x}} \\ \mathbf{x} \end{bmatrix} = \begin{bmatrix} \mathbf{F}_{N_g} \\ \mathbf{O} \end{bmatrix} \quad (13)$$

the resulting form is,

$$\begin{aligned} & \begin{bmatrix} \frac{1}{\Delta t} \mathbf{M}_g & \frac{1}{\Delta t} \mathbf{C}_g + \frac{1}{2} \mathbf{K}_g \\ \frac{1}{2} \mathbf{M}_g & \frac{1}{\Delta t} \mathbf{M}_g \end{bmatrix} \mathbf{q}^{n+1} \\ & + \begin{bmatrix} -\frac{1}{\Delta t} \mathbf{M}_g & -\frac{1}{\Delta t} \mathbf{C}_g + \frac{\mathbf{K}_g}{2} \\ \frac{1}{2} \mathbf{M}_g & -\frac{1}{\Delta t} \mathbf{M}_g \end{bmatrix} \mathbf{q}^n \\ & + \begin{bmatrix} -\mathbf{F}_{N_g} \\ \mathbf{O} \end{bmatrix} = \begin{bmatrix} \mathbf{O} \\ \mathbf{O} \end{bmatrix} \end{aligned} \quad (14)$$

Aerodynamic Model

To accurately model the aerodynamics of MiTEs, an unsteady Navier-Stokes computation is required. Such 3D, separated flow CFD requires large computational resources and is impractical for rapid aeroelastic analysis or control design. In spite of the complicated nonlinear phenomena with the MiTEs, the net aerodynamic forces and moments on the wing may be approximated well using an unsteady linear panel model, with some empirical inputs.

The aerodynamic model of the MiTE device used here consists of a single panel at the trailing edge that can change its boundary condition at the collocation point. The size of the flap, and consequently the number of chordwise panels, is selected so that it produces the same ΔC_l and $\Delta C_{m_{a.c.}}$ observed in various experiments and steady 2D CFD analysis.^{2,3}

Expressions for the ΔC_l and $\Delta C_{m_{a.c.}}$ can be derived using thin airfoil theory. These values are functions of the flap chord c_f and the flap deflection angle δ .

$$\Delta C_l = 2\pi \left(1 - \frac{\theta_f}{\pi} + \frac{1}{\pi} \sin \theta_f \right) \delta_{\max} \quad (15)$$

$$\begin{aligned} \Delta C_{m_{a.c.}} &= \frac{\Delta C_l}{4} \\ &- \left(\frac{\pi}{2} - \frac{\theta_f}{2} + \sin \theta_f - \frac{\sin 2\theta_f}{4} \right) \delta_{\max} \end{aligned} \quad (16)$$

where

$$\frac{c_f}{c} = \frac{1}{2} (1 - \cos \theta_f) \quad (17)$$

Thus, if the flap is small or θ_f is close to π , a simple expression for the ratio between $\Delta C_{m_{a.c.}}$ and $-\Delta C_l/4$ can be obtained.

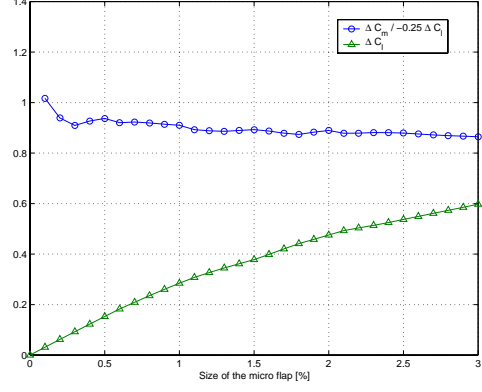


Figure 4: ΔC_l and $\frac{\Delta C_{m_{a.c.}}}{-\frac{1}{4}\Delta C_l}$ vs $\frac{c_f}{c}$

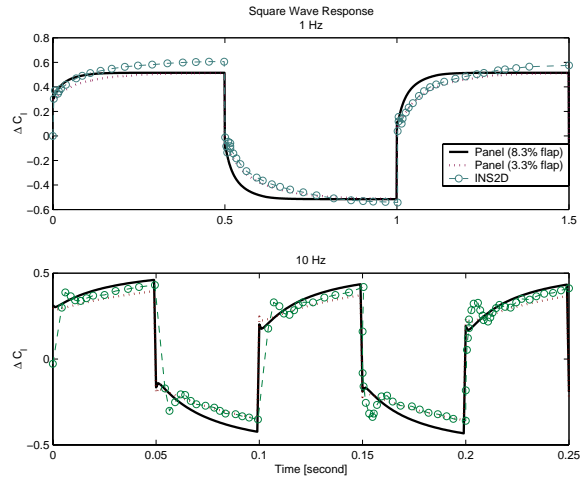


Figure 5: Unsteady 2-D flap response

$$\frac{\Delta C_{m_{a.c.}}}{(-\frac{1}{4}\Delta C_l)} \approx 1 - \frac{c_f}{c} \quad (18)$$

By looking at the ratio between $\Delta C_{m_{a.c.}}$ and $-\Delta C_l/4$, the effective flap size is determined. The required deflection of the flap is given by the value of ΔC_l , using Equation 15.

From experiments and simulations,^{2,3} this ratio is close to 0.9, which means the flap should be fairly small. Figure 4 is constructed using the data from Jang² and shows the ΔC_l and the ratio at zero angle of attack as a function of the flap size. As can be seen from Figure 4, the ratio is somewhat scattered around 0.9. For the current study $\Delta C_l = 0.4$ and $\frac{\Delta C_{m_{a.c.}}}{-\frac{1}{4}\Delta C_l} = 0.92$ are selected, which results in 12 chordwise panels. This choice corresponds to a MiTE flap of about 1.5% chord.

Modelling the flap with one panel flap turned out

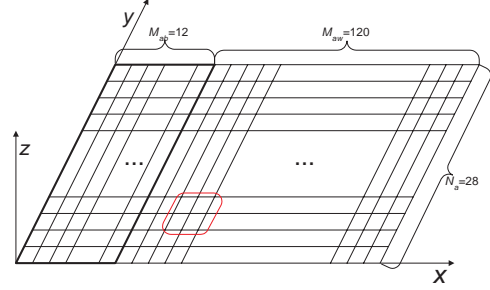
to be adequate in simulating the 2-D, unsteady aerodynamics of MiTEs. Figure 5 shows the lift coefficient of a 2-D section when the MiTEs are actuated with 1 Hz and 10 Hz square wave. The flaps are sized to provide steady state ΔC_l of 0.6. The INS2D CFD simulation was performed by Samy Elkayam. Both the INS2D and the panel computation shows the Wagner type lift build up in their responses but with slightly different time constants. The time constant is larger for the smaller panel and agrees more closely with the INS2D results.

The aerodynamic model is a discrete time domain unsteady vortex panel formulation derived from Hall,¹⁰ except that vortex ring elements¹² are used. This approach makes the detailed formulation simpler and increases the expandability of the analysis because it can be easily modified to include other effects such as camber. Figure 6 shows the panels and the relative placements of vortex ring elements. All the panels including the wake panels are assumed to lie in a single plane and have chordwise length Δx and spanwise width Δy . The model consists of 12 chordwise and 28 spanwise panels. The number of chordwise panels results from the above discussion of flap modelling. The number of spanwise panel is determined by the spanwise size of the MiTEs. The leading edge of the vortex ring is aligned with the quarter chord of the panel, and the trailing edge is aligned with the quarter chord of the next chordwise panel. Collocation points are located at the center of the three quarter chord line of each panel.

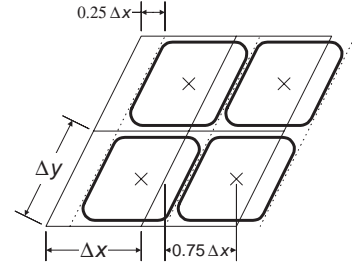
The basic equation of the vortex panel model can be written as Equation 19 where the variable $\mathbf{\Gamma}$ is the vector of circulations for all vortex rings including those at the wake panels. For the boundary condition \mathbf{W} , the first $M_{ab} \times N_a$ entries are the actual boundary conditions at the collocation points, and the remaining entries are zeros.

$$[AIC]\mathbf{\Gamma} = \mathbf{W} \quad (19)$$

The deformation and the motion of the wing from the finite element analysis are reflected as changing the boundary conditions since the panels are assumed to be fixed. Using the shape functions, the outward normal at each collocation point can be found from the nodal degrees of freedom. In addition, the change in boundary conditions due to the flaps are added. As the flaps are not pushing the flow, but rather cutting into the flow, the velocity and the acceleration of the flaps are ignored in the aerodynamic model of the flap. In matrix form,



(a) Panel layout



(b) Enlarged view with vortex ring elements

Figure 6: Grid for vortex panel method

$$\mathbf{W}^n = [WDR]\mathbf{q}^n + [WDR_c]\delta^n \quad (20)$$

The strength of the first wake vortices can be found by Kelvin's theorem, which states that the strength of the unsteady vorticity shed in the wake is proportional to the time rate of change of total circulation around the airfoil. In the case of vortex ring element, Kelvin's theorem is equivalent to the last bound vortex ring simply convected to the wake. As all the wake vortices are convected with the freestream velocity, we can write,

$$\Gamma_{i,j}^{n+1} = \Gamma_{i-1,j}^n \quad \text{for } i = M_{ab} + 1, \dots, M_a - 1 \quad (21)$$

where the time step is,

$$\Delta t = \frac{\Delta x}{U_\infty} \quad (22)$$

Because the computational model has a finite length wake, special treatment is required at the last vortex element to prevent the starting vortex from disappearing at the end of the wake.¹⁰

$$\Gamma_{M_a,j}^{n+1} = \Gamma_{M_a-1,j}^n - (1 - \alpha)\Gamma_{M_a,j}^n \quad (23)$$

where α is a relaxation factor, which is normally $0.95 < \alpha < 1.0$.

Putting together the three relations and casting into matrix form gives,

$$[CDR_2] \mathbf{\Gamma}^{n+1} + [CDR_1] \mathbf{\Gamma}^n = \mathbf{W}^n \quad (24)$$

Finally the pressure difference between the upper and the lower surface of each panel is found using the unsteady Bernoulli's equation.

$$\Delta P_{i,j}^{n+\frac{1}{2}} = \frac{\rho U}{\Delta x} \left(-\frac{1}{2} \Gamma_{i-1,j}^{n+1} + \frac{3}{2} \Gamma_{i,j}^{n+1} - \frac{1}{2} \Gamma_{i-1,j}^n - \frac{1}{2} \Gamma_{i,j}^n \right) \quad (25)$$

In matrix form

$$\Delta \mathbf{P}^{n+\frac{1}{2}} = [C2P_2] \mathbf{\Gamma}^{n+1} + [C2P_1] \mathbf{\Gamma}^n \quad (26)$$

The pressure difference is combined with the Equation 8 from the FEM formulation to calculate the nodal forces.

Flutter Analysis

The flutter model combines the previously mentioned finite element method for structural analysis with the vortex panel method for aerodynamics. The pressure differences between the upper and lower surfaces of panels are translated to nodal forces acting on the structure. The nodal deformations from the finite element model are translated to the boundary conditions of the panels. The strength of the vortices and the nodal degrees of freedom are combined into a single large state vector. Eigenvalues and eigenvectors are computed to determine the stability of the combined aero-structural system. The discrete time domain mathematical model is composed of four basic parts.¹⁰

- Circulation - Downwash relation from the vortex panel method, Equation 24.

$$[CDR_2] \mathbf{\Gamma}^{n+1} + [CDR_1] \mathbf{\Gamma}^n = \mathbf{W}^n$$

- Circulation - Nodal force relation from the unsteady Bernoulli equation and work equivalent load method, Equation 26 and 8.

$$\mathbf{F}^{n+\frac{1}{2}} = [CNFR_2] \mathbf{\Gamma}^{n+1} + [CNFR_1] \mathbf{\Gamma}^n$$

- Wing motion - downwash relation and the actuator model from the geometry, Equation 20.

$$\mathbf{W}^n = [WDR] \mathbf{q}^n + [WDR_c] \delta^n$$

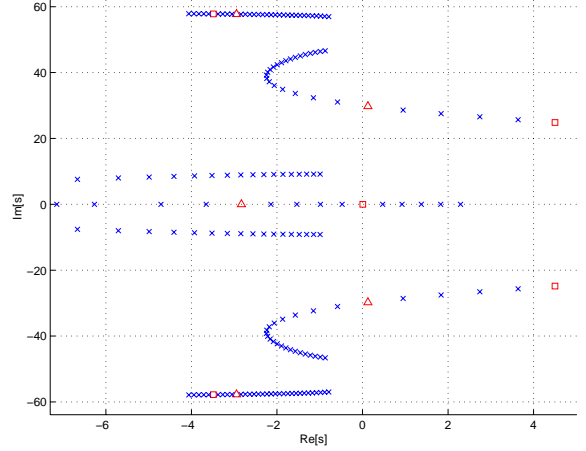


Figure 7: Root Locus of three lowest frequency modes

- Discretized equation of motion from the finite element formulation, Equation 14.

$$[DEOM_2] \mathbf{q}^{n+1} + [DEOM_1] \mathbf{q}^n + \mathbf{F}^{n+\frac{1}{2}} = \mathbf{O}$$

Finally we have complete state space equation in discrete time form.

$$\begin{aligned} & \begin{bmatrix} [CDR_2] & -[WDR] \\ [CNFR_2] & [DEOM_2] \end{bmatrix} \begin{bmatrix} \mathbf{\Gamma} \\ \mathbf{q} \end{bmatrix}^{n+1} \\ & + \begin{bmatrix} [CDR_1] & [O] \\ [CNFR_1] & [DEOM_1] \end{bmatrix} \begin{bmatrix} \mathbf{\Gamma} \\ \mathbf{q} \end{bmatrix}^n \\ & = \begin{bmatrix} [WDR_c] \\ [O] \end{bmatrix} \delta^n \quad (27) \end{aligned}$$

Flutter analysis can be done by computing the eigenvalues of the system with zero input. With this discrete time formulation, the instability occurs when there exists at least one eigenvalue which has magnitude greater than one. Furthermore, the eigenvalues can be converted to continuous time domain by taking the natural logarithm and dividing by the time step.

Figure 7 shows the root locus of the three lowest frequency structural modes starting with a flow speed of 4 m/s. The wing flutters at approximately 15.5 m/s with frequency of 4.8 Hz and diverges at about 17.5 m/s, which agrees well with the wind tunnel results of 14 m/s for the flutter speed and 5 Hz for the flutter frequency.

Control

The flap is basically an open loop servo mechanism. There are only two types of command to the flaps,

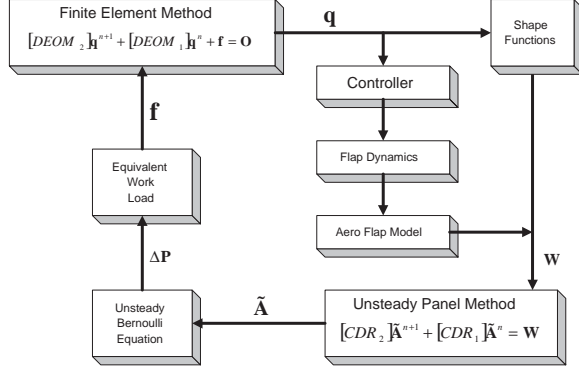


Figure 8: Overall structure of the analysis

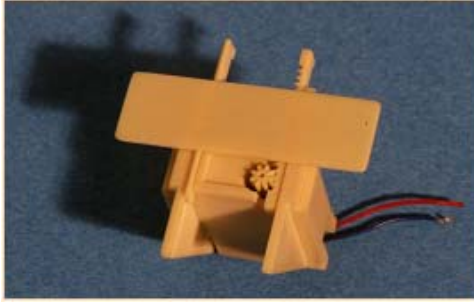


Figure 9: A photo of current MiTE actuator

up and down. For example, this can be the voltage applied to the DC motor that actuates the flap, $+V_{\max}$ or $-V_{\max}$. The final positions of the flaps can be varied according to the locations of stops. In this study two types of flaps were considered that can move from neutral to up, and another neutral to down. The ability to command neutral is important for two reasons: (i) Due to the high control effectiveness of the flaps, only impulsive actuation is required to stabilize the wing, (ii) and to minimized the drag penalty, the flaps should be in the neutral position as much as possible.

The dynamic model of the actuator is a sliding mass with linear friction, controlled by a force which has either of two values, $\pm F_f$, where the range of the movement is restricted.

$$\begin{cases} 0 \leq h_f \leq l_f & \text{up-neutral flap} \\ -l_f \leq h_f \leq 0 & \text{down-neutral flap} \end{cases}$$

The parameters were chosen such that the model has the same time constant as obtained from the actual tests of the actuators. Figure 9 is the photo of current actuator. The inertial effect from the flap to the wing is neglected when incorporating the dy-

mass (m_f)	5.1647×10^{-4} Kg
friction (b_f)	5.1647×10^{-4} Kg/s
force (F_f)	6.1679×10^{-3} N
moving range ($2l_f$)	1.8510×10^{-3} m
bandwidth	20 Hz

Table 3: Actuator parameters

amic model of the flap into the finite element model of the wing, since the mass of the flap is considerably smaller. The time required for the flap to move from full down to full up is 24.75 msec. Including flap dynamics resulted in more accurate modelling and prevented the optimizer from converging to a non-realistic solution that involves flaps actuating in very high frequencies. Table 3 details the choice of parameters for the actuator.

The governing equation for the flap dynamics can be summarized as Equation 28. The middle term at the right hand side is the inertial influence from the wing to the flap.

$$\mathbf{q}_f^{n+1} = \mathbf{A}_f \mathbf{q}_f^n - m_f \mathbf{A}' \dot{\mathbf{q}}^n + \mathbf{B}_f f_f^n \quad (28)$$

There exists a separate aerodynamic model for the actuator, which is just a small conventional flap discussed in the aerodynamics section. The deflection angle of this aerodynamic flap will be set according to the position of the flap from the dynamic model.

$$\delta_j = \begin{cases} \frac{\delta_{\max}}{l_f} h_j & (|h_j| \geq 0.1l_f) \\ 0 & (|h_j| < 0.1l_f) \end{cases} \quad (29)$$

As the sliding flap always maintains nearly 90 degrees angle to the flow, the aerodynamic effectiveness with respect to the position of the flap scales as in Figure 4. Though the effectiveness of the flap is not exactly linear with the size of the flap, the curve between the range $0 \leq \Delta C_l \leq 0.4$ can be approximated by a linear relation. Also, there exists a small dead band, if the height of the flap is smaller than the thickness of the trailing edge. That is, the flap should move a certain amount to stick out from the trailing edge. In this study, the dead band is assumed to be 10% of its full movement range.

As in Figure 10, there are 28 slots along the entire trailing edge where 26 flaps are attached, excluding the slots located at the root and the tip. Up-type and down-type flaps are alternating where the flap nearest to the tip is down-type. Two flaps act as a pair such that if the pair receives an up command, the up-type flap goes up, while the down type goes neutral. For down command, it is the inverse of the

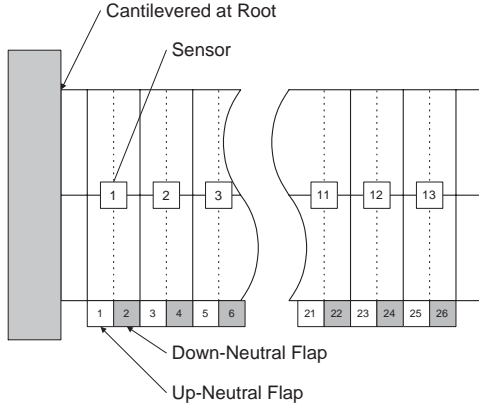


Figure 10: Sensor and actuator layout

up command case, and for neutral command, both flaps are at the neutral position. Using this approach 13 pairs of flaps will be commanded according to their local sensor measurements.

Along with the control design, the sensor configuration is also examined. The wing is divided into 13 spanwise sections where every section has its own pair of actuators and the spanwise location of the sensor is in between the two actuators. The sensor for each section is located at the mid chord. Local measurements from each section are passed through a first order low pass filter with cut off frequency of 32 Hz, and are fed back to the local pair of actuators. As the individual actuator takes only one of the two inputs, $+F_f$ or $-F_f$, the signal from the controller is filtered by a relay. For the up-neutral type flap, the switching threshold of the relay is $+u_{thres}$ while $-u_{thres}$ is used for the down-neutral type flap. The control scheme is summarized in Figure 11.

Four basic measurements were examined, deflection, rate of deflection, twist, and rate of twist. The study showed that by only measuring the rate of twist it was possible to stabilize the wing when the flow speed is between the flutter speed and the divergence speed. If the flow speed is higher than the divergence speed, twist rate feedback stabilizes the wing only for a short period of time. This suggests that even though the flutter mode can be stabilized by only using rate of twist feedback, the divergence mode is still driving the closed loop system unstable. By adding deflection feedback, the whole system was successfully stabilized. The study showed that in stabilizing the divergence mode, using cube of the deflection was much more effective than the deflection itself. The complete control law is then,

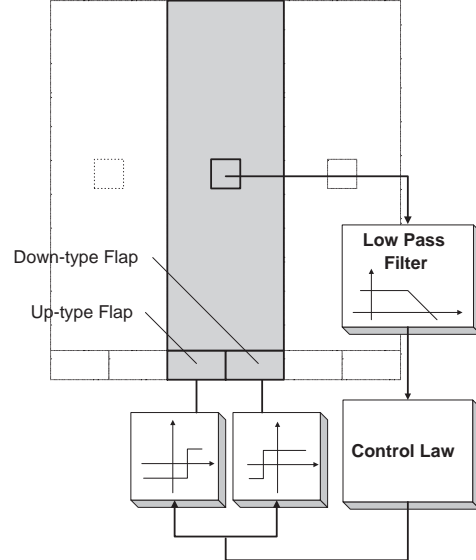


Figure 11: Control scheme

$$u = K_h h^3 + K_{\dot{\theta}} \dot{\theta} \quad (30)$$

The switching thresholds, u_{thres} , are fixed to ± 1 and the optimal gains for the control law were found by using a non-linear simplex optimizer with time domain integration. The nonlinearity of the actuator prevents using the conventional control techniques such as LQR. The objective function was set as the square sum of the degrees of freedom, normalized by their prescribed maximum values. To provide the optimizer with a smooth objective, a penalty function was added which limits the maximum displacement. If the displacement at the tip mid chord exceeded a specific maximum, in this case the chord length, before completion of the integration, the integration was terminated and the square of the remaining time was added to the objective.

$$J = \sum_{i=0}^{N_p} \hat{\mathbf{x}}_i^T \hat{\mathbf{x}}_i + w (t_f - t_p)^2 \quad (31)$$

The initial condition for the time domain integration is loading the tip leading edge of the wing with a small load of 0.3 N to excite both the bending and torsion modes.

For the flow speed smaller than the divergence speed, there exists a wide range of $K_{\dot{\theta}}$ that stabilizes the wing. For flow speed larger than the divergence speed, using $K_h = 25000$ and $K_{\dot{\theta}} = 2.554$, stabilized the wing up to a flow speed of 18.9 m/s, which is 22% above the flutter speed. Figure 12 shows the

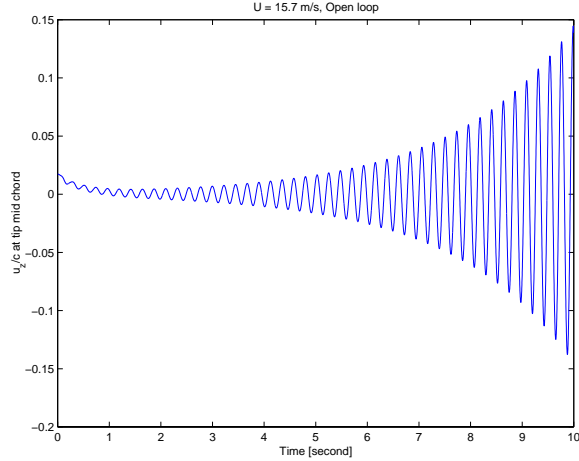


Figure 12: Open loop time history of tip mid chord when $U_\infty = 15.7$ m/s

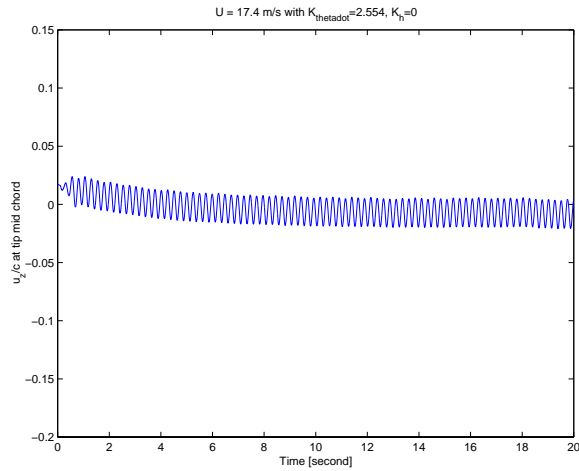


Figure 13: Closed loop time history of tip mid chord when $U_\infty = 17.4$ m/s with rate of twist feedback only

time history of the mid chord wing tip deflection for 10 seconds at a flow speed of 15.7 m/s, which is slightly larger than the flutter speed and no control is applied.

Figure 13 shows the closed loop response drawn to the same scale as Figure 12 for 20 seconds. In this case, the flow speed is 17.4 m/s which is slightly smaller than the divergence speed. The wing is successfully stabilized to a small magnitude limit cycle oscillation by only using the twist rate feedback.

Finally, Figure 14 show the motion of the wing tip mid chord at the maximum stabilizable flow speed of 18.9 m/s found by this study.

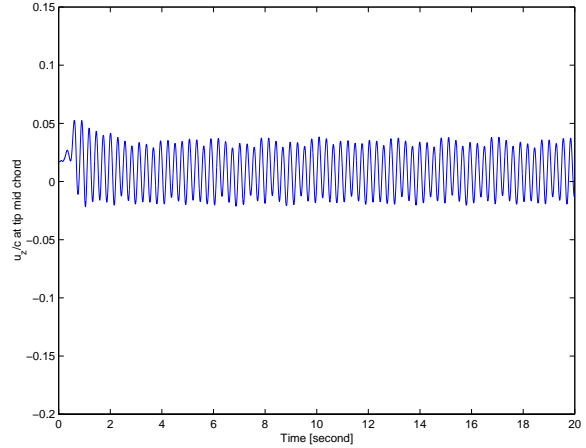


Figure 14: Closed loop time history of tip mid chord when $U_\infty = 18.9$ m/s

Conclusions

The use of multiple small trailing edge devices for aeroelastic control was evaluated using a linear structural analysis and time-dependent aerodynamic model. Unsteady aerodynamic phenomena limit the effective bandwidth of these devices, but even with a simple control law, it was possible to increase the flutter dynamic pressure significantly. Current work involves improved aerodynamic modelling and the experimental validation of these results along with an investigation of new approaches to control law design for these systems.

Acknowledgments

Mr. Samy Elkayam is greatly acknowledged for providing CFD results which were invaluable for the aerodynamic analysis. Dr. Dan Borglund is acknowledged for his many contributions when he involved as a postdoctoral candidate on the project. The project was financially supported by Air Force Office of Scientific Research (AFOSR). The first author was financially supported by Stanford Graduate Fellowship (SGF).

References

- [1] Liebeck, R. H., "Design of Subsonic Airfoils for High Lift", Journal of Aircraft, Vol. 15, No. 9, September 1978.

- [2] Jang, C. S., Ross, J. C., and Cummings, R. M., "Computational Evaluation of an Airfoil with a Gurney Flap", AIAA Paper 92-2708, June 1992.
- [3] Storms, B. L. and Jang, C. S., "Lift Enhancement of an Airfoil Using a Gurney Flap and Vortex Generators", Journal of Aircraft, Vol. 31, No. 3, June 1994.
- [4] Giguere, P., Lemay, J., and Dumas, G., "Gurney Flap Effects and Scaling for Low-Speed Airfoils", AIAA Paper 95-1881, June 1995.
- [5] Jeffrey, D., Zhang X., and Hurst, D. W., "Aerodynamics of Gurney Flaps on a Single-Element High-Lift Wing", Journal of Aircraft, Vol. 37, No. 2, 2000, pp. 295-301.
- [6] Zerihan, J., Zhang X., "Aerodynamics of Gurney Flaps on a Wing in Ground Effect", AIAA Journal, Vol. 39, No. 5, May 2001, pp. 772-780.
- [7] Kroo, I. M., Eaton, J., and Prinz, F., "UAV Aeroelastic Control Using Redundant Microflaps", AFOSR Program Review for Year I, 1999.
- [8] Kroo, I. M., "Aerodynamic Concepts for Future Aircraft", 30th AIAA Fluid Dynamics Conference (AIAA-99-3524), Norfolk, VA, June-July 1999.
- [9] Borglund, D., and Kroo, I. M., "Aeroelastic design optimization of the micro trailing edge flap flexible wing", CEAS/AIAA/AIAE International Forum on Aeroelasticity and Structural Dynamics, Madrid, Spain, June 2001.
- [10] Hall, K. C., "Eigenanalysis of Unsteady Flows About Airfoils, Cascades, and Wings", AIAA Journal, Vol. 32, No. 12, 1994, pp. 2426-2432.
- [11] Przemieniecki, J. S., Theory of Matrix Structural Analysis, McGraw-Hill, New York, 1968.
- [12] Katz, J., Plotkin, A., LOW-SPEED AERODYNAMICS: From Wing Theory to Panel Methods, McGraw-Hill, Singapore, 1991.